Supporting Information

Medium–entropy iron–series metal sulfide for energy–saving hydrogen production and highly–efficient direct hydrazine borane fuel cell

Hao Zhou,[a] Cuiqing Zhang,[a] Minsong Huang,[a] Yixing Luo,*[b] and Zhang–Hui Lu*[a]

[a] Key Laboratory of Green Catalysis of Jiangxi Education Institutes, Key Laboratory of Energy Catalysis and Conversion of Nanchang, College of Chemistry and Materials, Jiangxi Normal University, Nanchang 330022, China

[b] Jiangxi Academy of Eco–Environmental Sciences and Planning, Jiangxi Key Laboratory of Environmental Pollution Control, Nanchang 330039, China

*E–mail: luzh@jxnu.edu.cn (Zhang–Hui Lu); xingyiluo@foxmail.com (Yixing Luo)

Table of Content

Experimental section

Materials and reagents

All chemicals were obtained from commercial sources. Hydrazine hemisulfate salt ($N_2H_4 \cdot 1/2H_2SO_4$, Aldrich, 98%), sodium borohydride ($NaBH_4$, Aladdin, 99.5%), nickel nitrate hexahydrate ($Ni(NO_3)_2 \cdot 6H_2O$, Aladdin, 98%), cobalt nitrate hexahydrate ($Co(NO_3)_2 \cdot 6H_2O$, Aladdin, 99.9%), ammonium fluoride (NH_4F, Macklin), Iron nitrate nonahydrate ($Fe(NO_3)_3 \cdot 9H_2O$, Aladdin, 98%), urea (H_2NCONH_2, Aladdin, 98%), hydrochloric acid (HCl, Aladdin, 37%), Pt/C (TEC10E20E, Tanaka), nickel foam (1.0 mm, Kunshan Lv Chuang), carbon paper (TGP–H–060, Toray) were used as received without further treatment. Hydrazine borane ($N_2H_4BH_3$) was synthesized according to our previous reported study.[S1] Ultrapure water used in the experiment was purified using a Millipore system. The anion ion exchange member (FAA–3–50, Fumasep) was treated with 1 M KOH solution for 24 h prior to utilization.

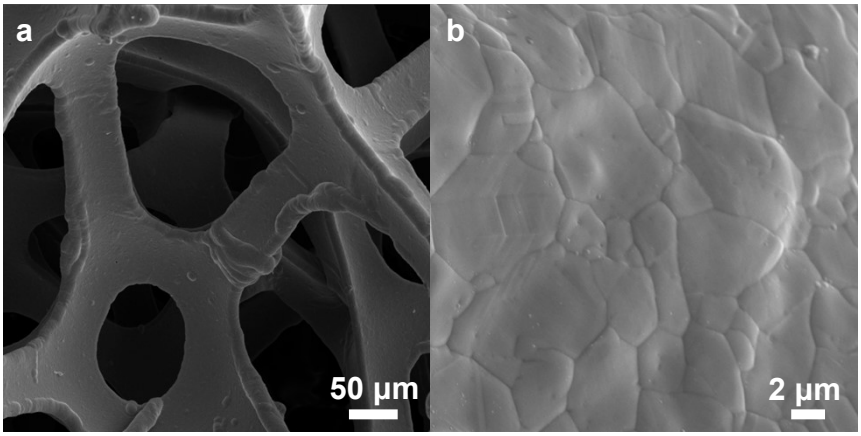

Figure S1. SEM images of NF.

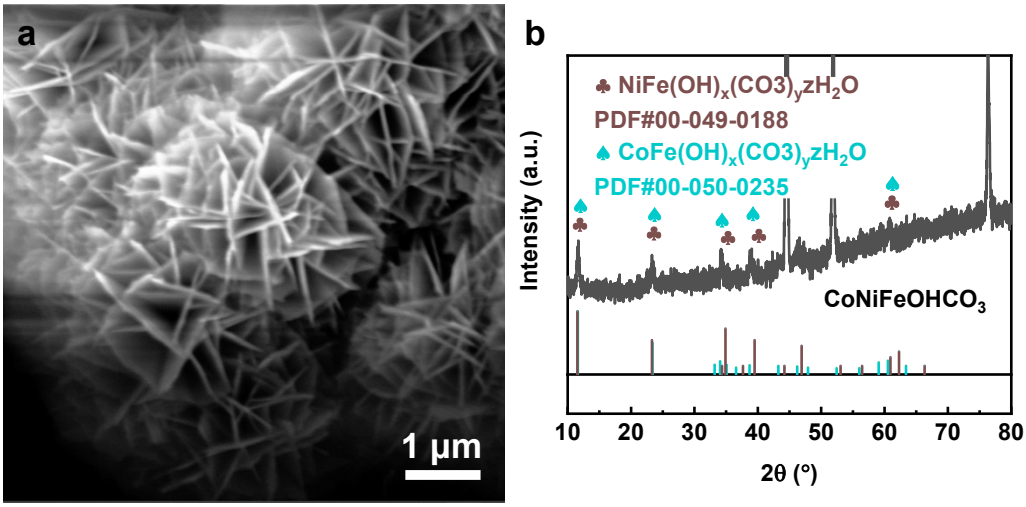

Figure S2. (a) SEM image and (b) XRD pattern of $CoNiFeOHCO_3$.

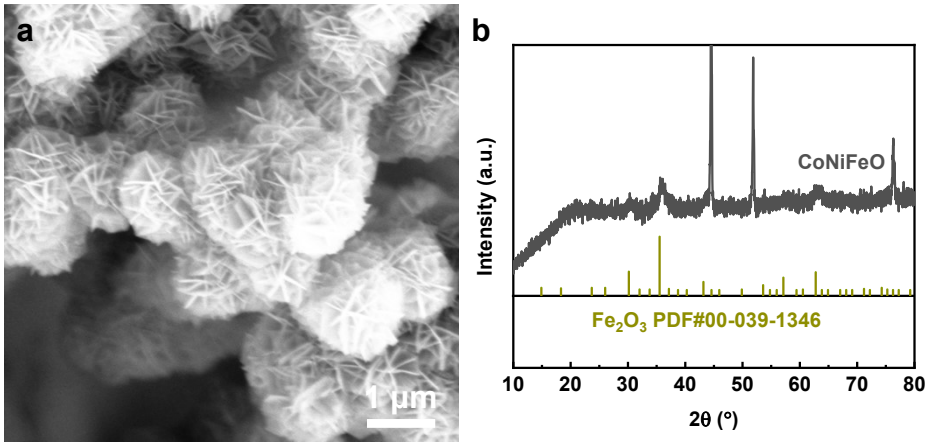

Figure S3. (a) SEM image and (b) XRD pattern of CoNiFeO.

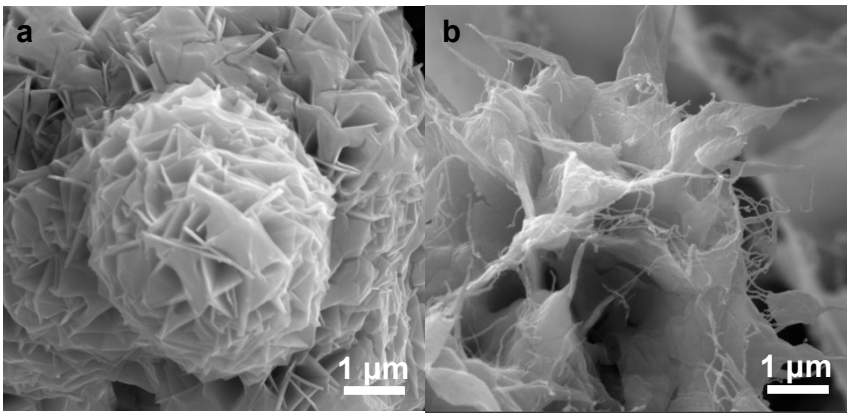

Figure S4. SEM images of (a) NiFeS and (b) CoS.

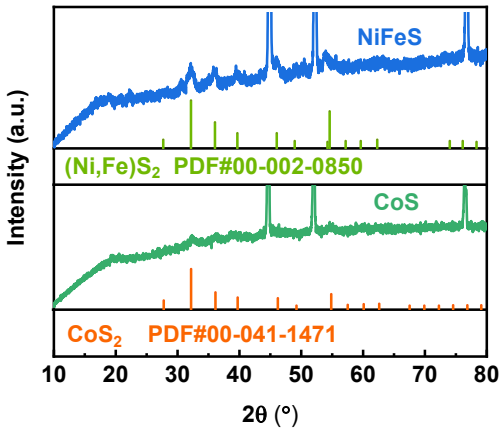

Figure S5. XRD patterns of NiFeS and CoS.

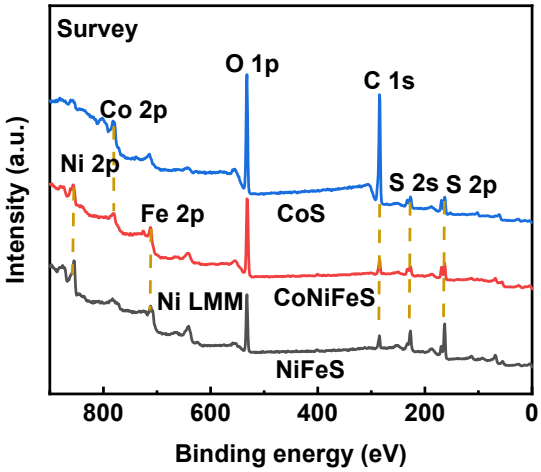

Figure S6. XPS survey spectra of CoNiFeS, NiFeS, and CoS.

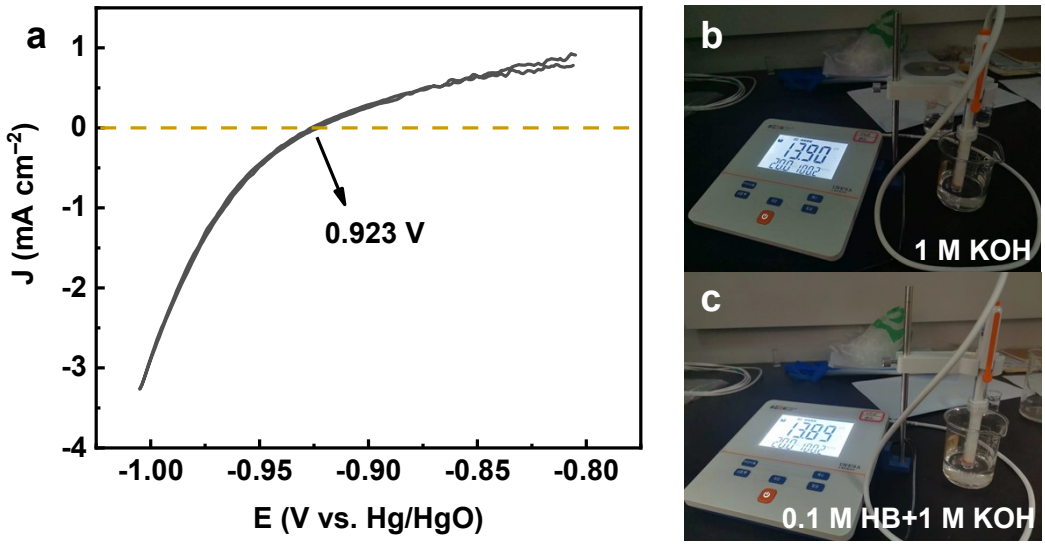

Figure S7. (a) Calibration of Hg/HgO reference electrode in 1 M KOH. The corresponding digital photographs of *pH* value in (b) 1 M KOH solution and (c) 1 M KOH + 0.1 M HB solution. All the potentials were calculated to the reversible hydrogen electrode (RHE) by the equation: $E_{RHE} = E_{Hg/HgO} + 0.923$ V.

Calibration of the Hg/HgO reference electrode was performed in H_2 saturated 1 M KOH using a three electrodes system: two 1.0 cm^2 Pt electrode served as working and counter electrodes, respectively. The Hg/HgO electrode acted as the reference. Cyclic voltammetry was recorded at 5 mV s^{-1}.

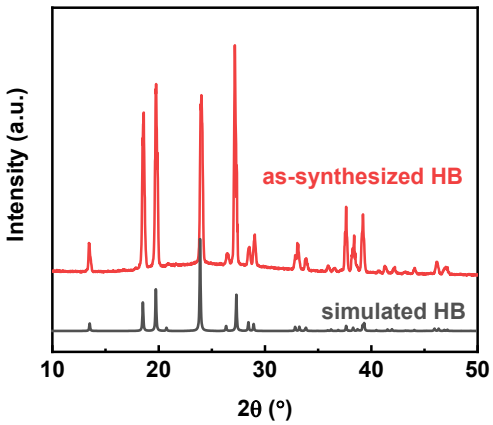

Figure S8. XRD patterns of home–made HB and simulated HB.

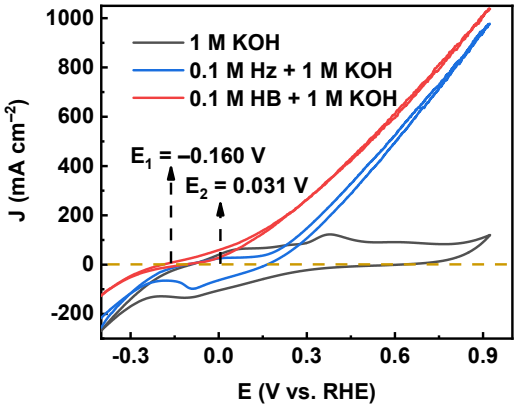

Figure S9. CV curves of HBOR and HzOR.

As shown in **Figure S9**, CV tests were conducted in 0.1 M HB + 1 M KOH and 0.1 M Hz + 1 M KOH, respectively. Compared to HzOR (E_{onset} = 0.031 V), the HBOR (E_{onset} = –0.160 V) exhibits a much lower onset potential and delivers much larger oxidation currents across the same potential range. All these results indicate that the HBOR is more thermodynamically favorable on the CoNiFeS catalyst, which is greatly beneficial for the practical applications in both energy–saving hydrogen production and direct liquid fuel cell systems.

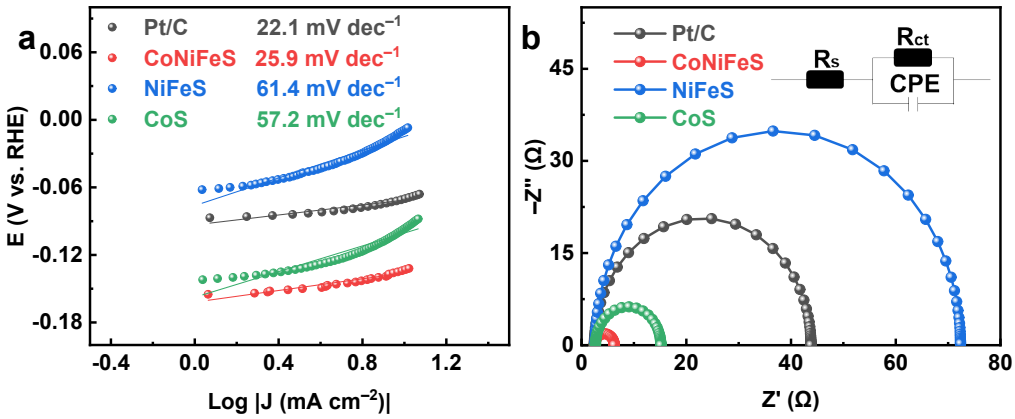

Figure S10. (a) Tafel plots and (d) Nyquist plots of as–prepared catalysts for HBOR, which were recorded at a potential of –0.12 V vs. RHE.

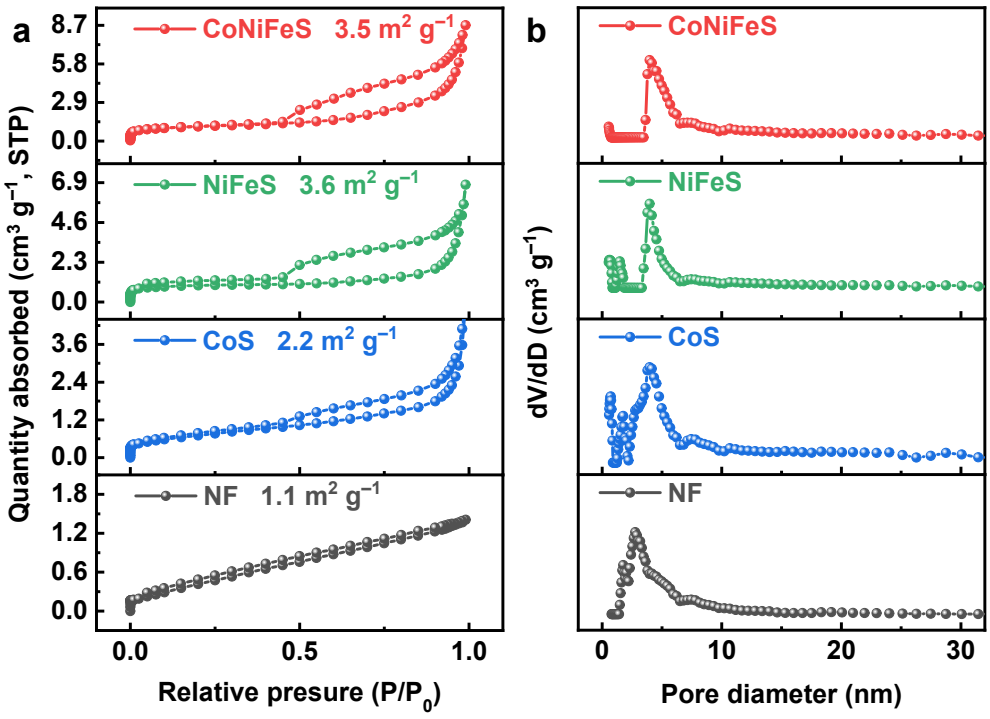

Figure S11. (a) Nitrogen adsorption–desorption isotherms and (b) pore size distribution of nickel foam self–supported catalysts.

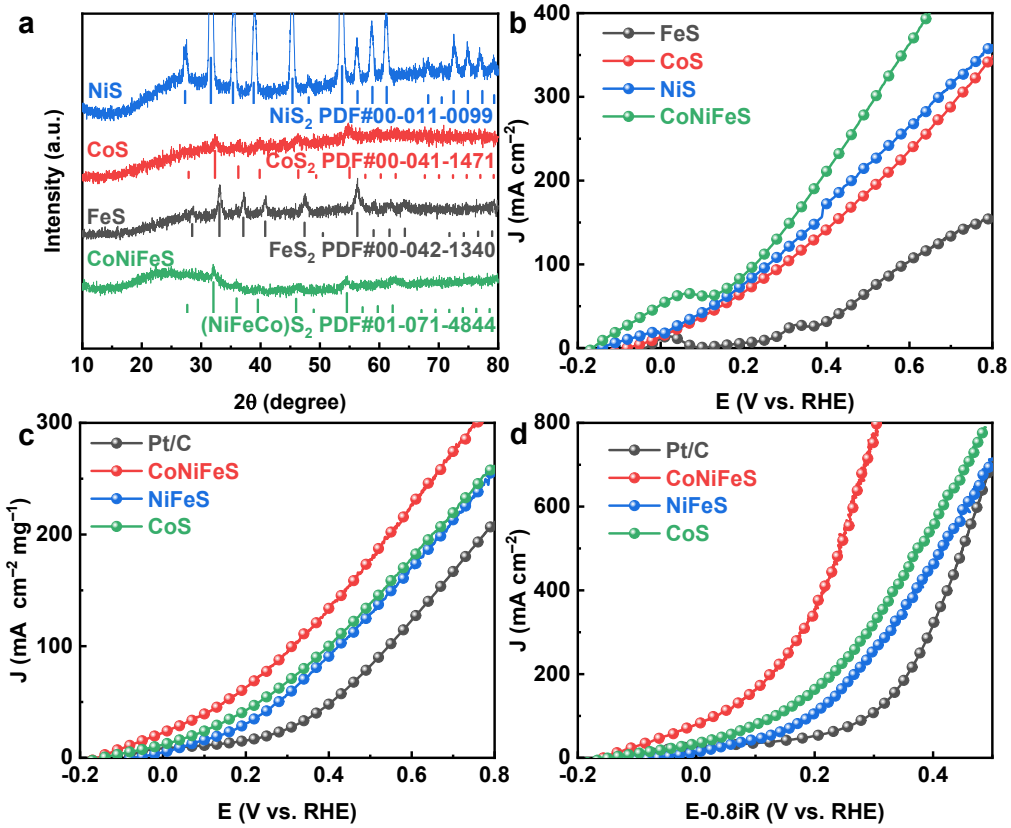

Figure S12. (a) XRD pattern and (b) HBOR performance of FeS, CoS, NiS, and CoNiFeS. (c) Comparison of mass–activity–normalized current densities, and (d) Comparison of 0.8iR–corrected polarization curves.

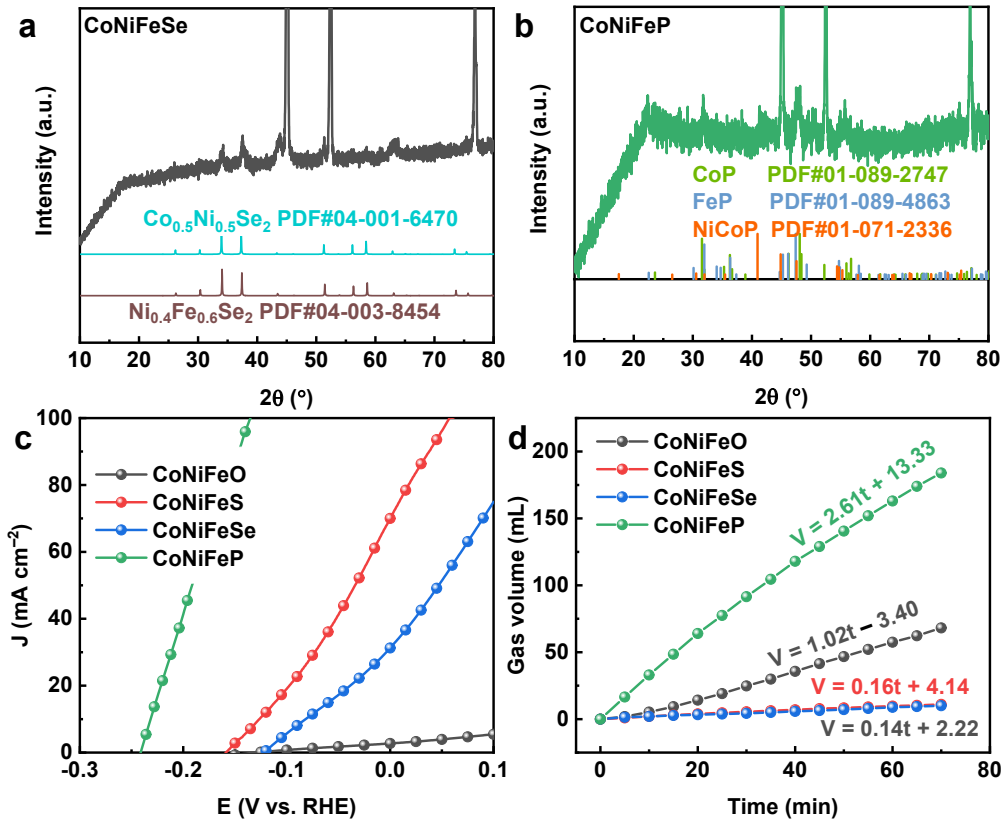

Figure S13. XRD patterns of (a) CoNiFeSe and (b) CoNiFeP. Comparation of CoNiFeX (X=O, S, Se, and P) for (c) HBOR and (d) HB hydrolysis in 1 M KOH + 0.1 M HB.

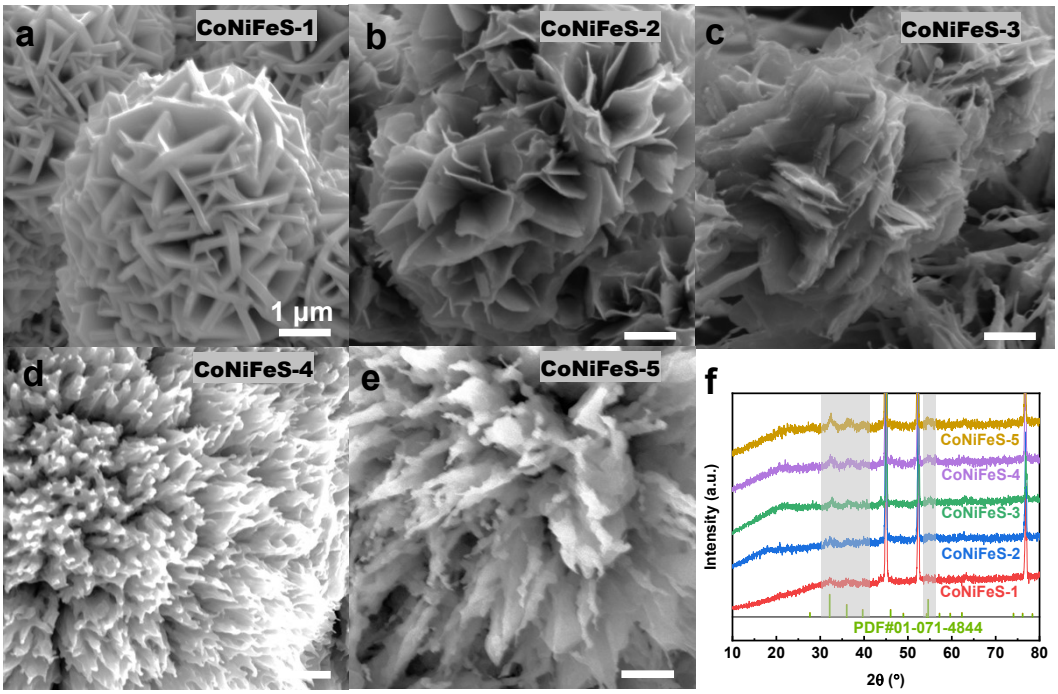

Figure S14. (a–e) SEM images and (f) XRD pattern for CoNiFeS–X (X=1–5).

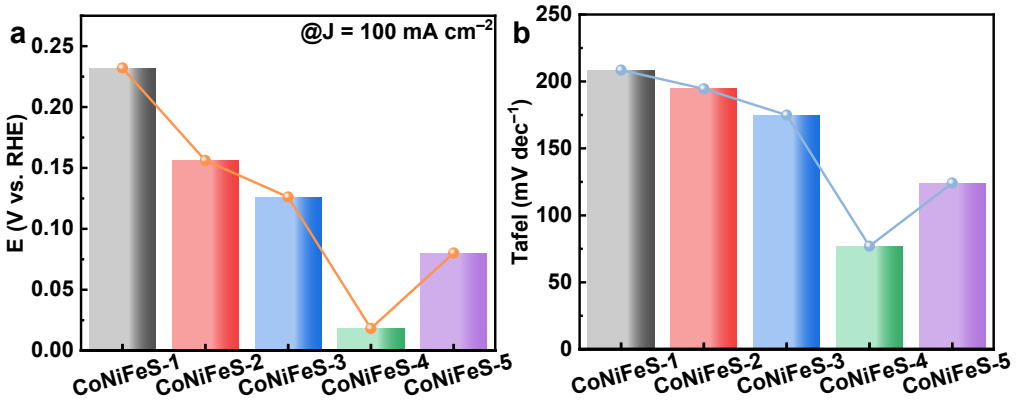

Figure S15. Comparation of the (a) potential values at 100 mA cm^{-2} and (b) Tafel slopes of CoNiFeS–X (X=1–5) for HBOR.

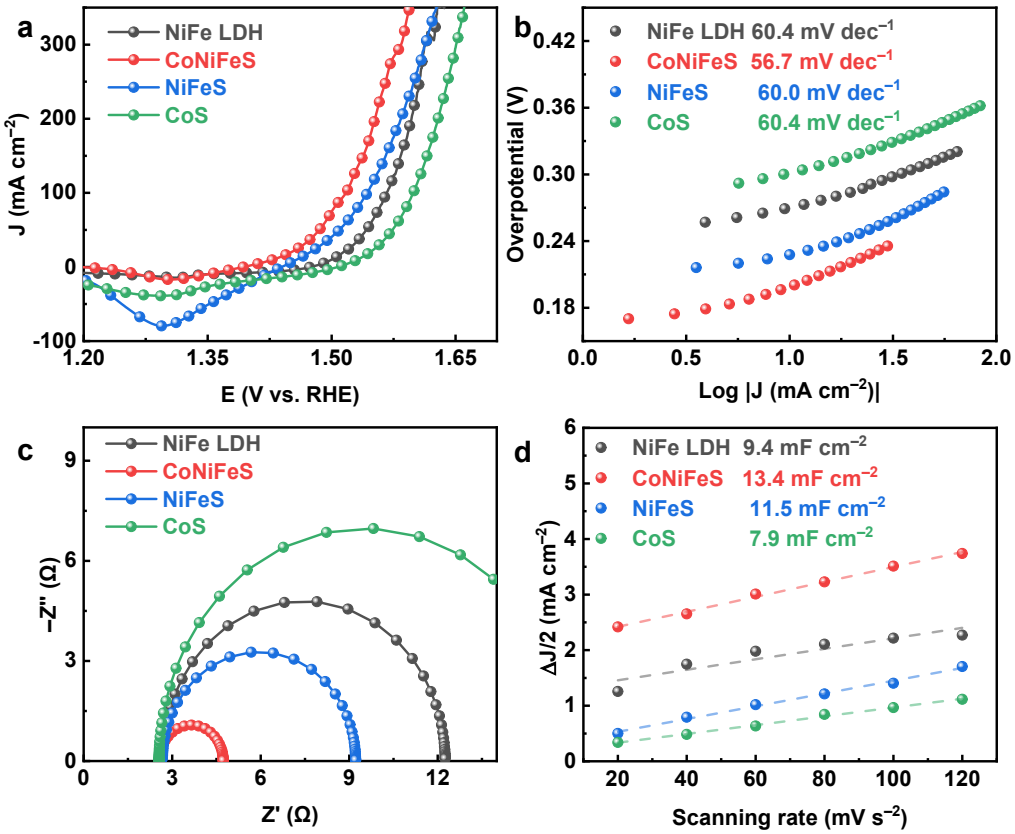

Figure S16. Electrochemical performance of CoNiFeS, NiFeS, CoS, and NiFe LDH: (a) LSV curves with 80% iR_s compensation for OER, (b) Tafel slopes, (c) Nyquist plots, and (d) Double–layer capacitance C_{dl}.

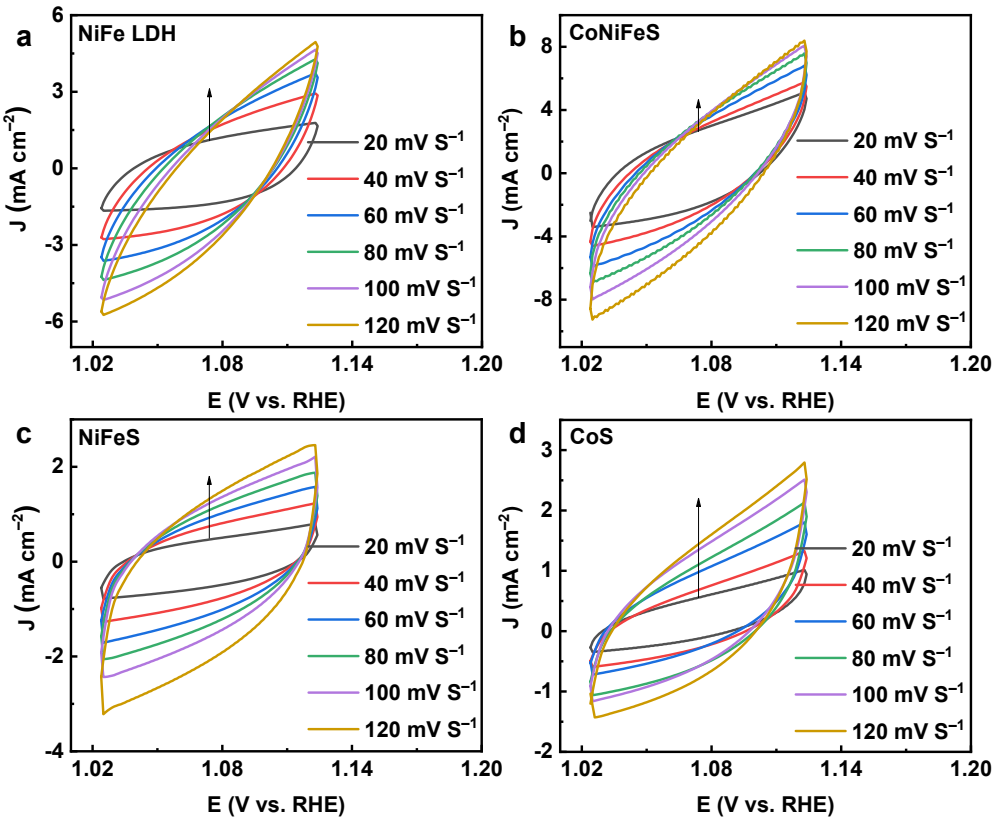

Figure S17. CV curves of (a) NiFe LDH, (b) CoNiFeS, (c) NiFeS, (d) NiFe LDH measured in the potential range of 1.024–1.124 V vs. RHE at different scan rates in 1 M KOH.

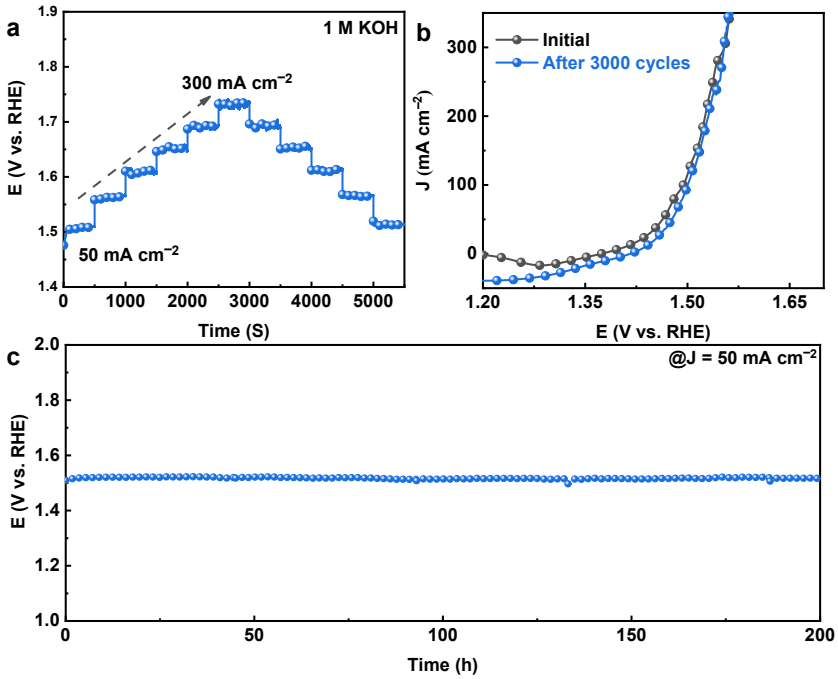

Figure S18. Electrochemical stability tests of CoNiFeS: (a) ADTs plots after 3000 cycles, (b) Multi–current stability: 50–300 mA cm^{-2}, (c) V–t stability at 50 mA cm^{-2}.

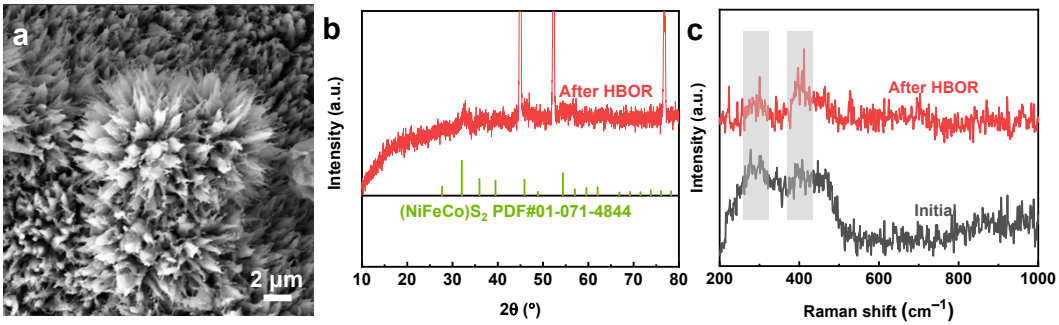

Figure S19. Characterizations of CoNiFeS after HBOR stability test: (a) SEM image, (b) XRD pattern, and (c) Raman spectra.

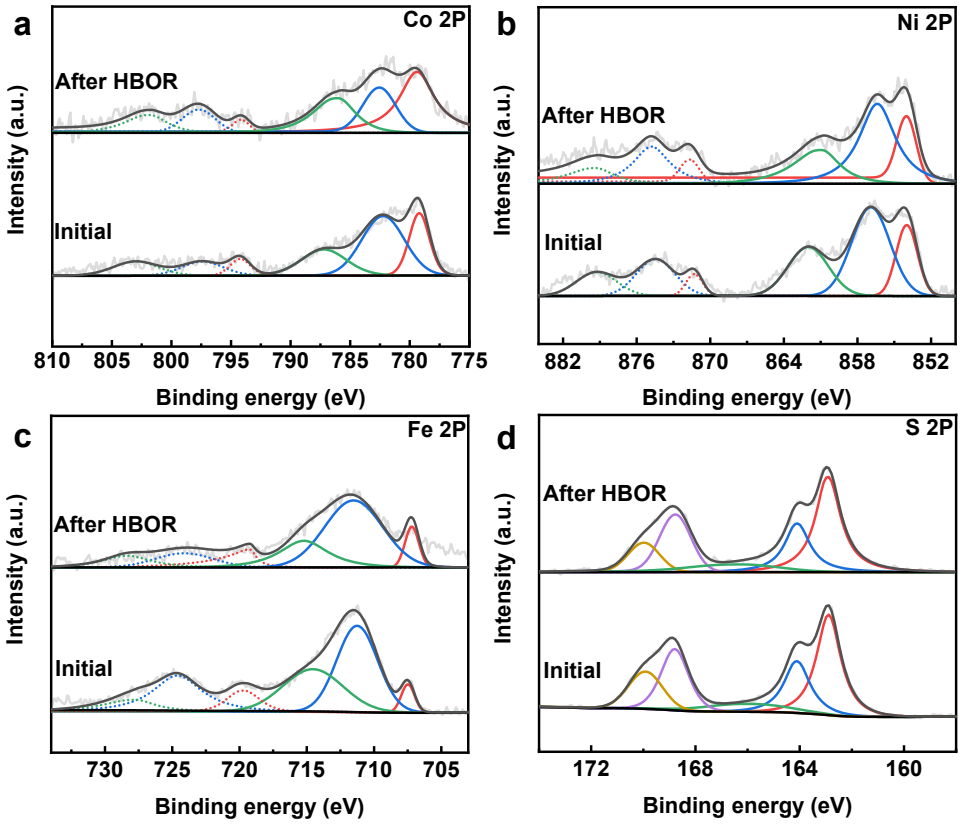

Figure S20. Comparison of XPS characterizations before and after HBOR stability test.

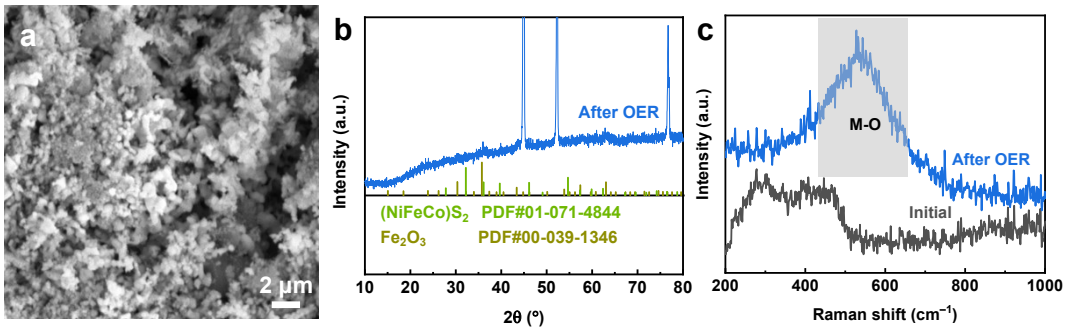

Figure S21. Characterizations of CoNiFeS after OER stability test: (a) SEM image, (b) XRD pattern, and (c) Raman spectra.

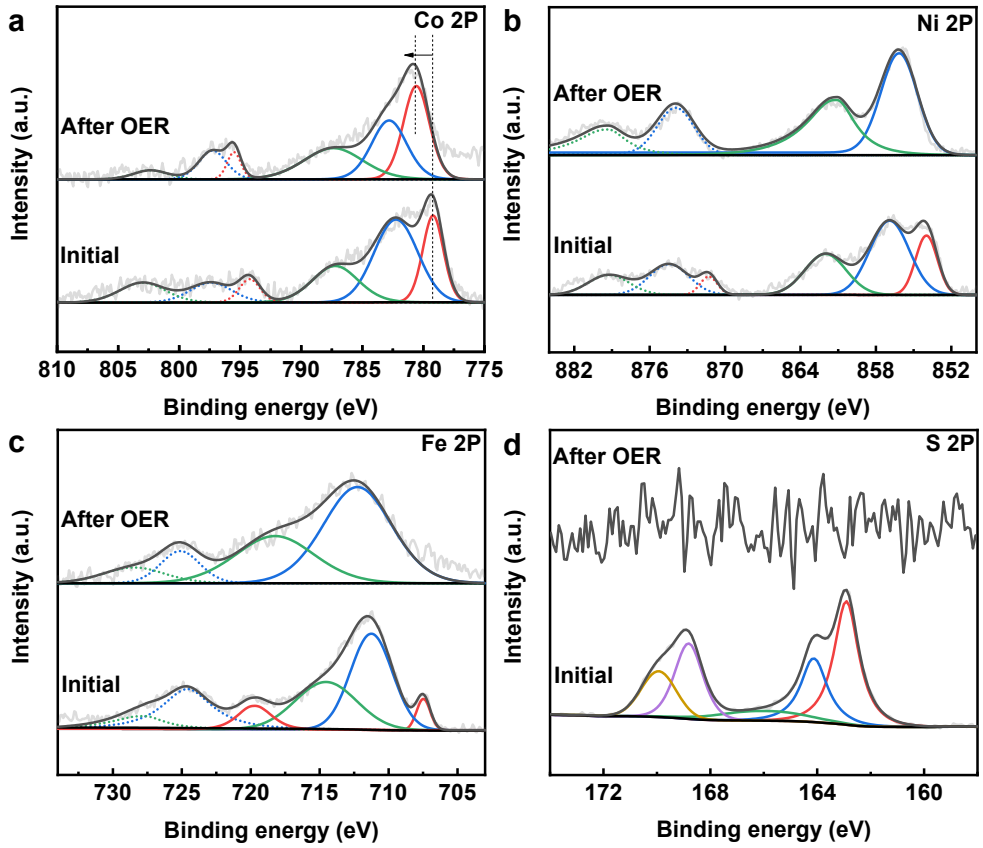

Figure S22. Comparison of XPS characterizations before and after OER stability test.

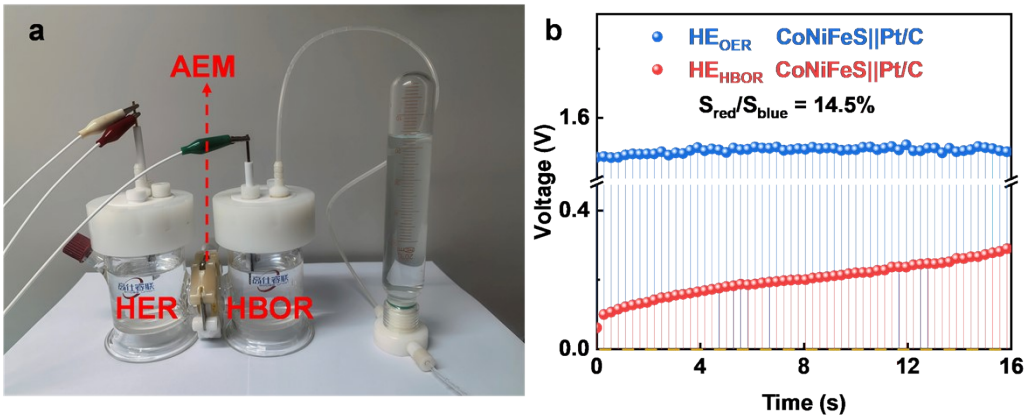

Figure S23. (a) Photograph of H–type cell for HE_{HBOR} and HE_{OER} tests, (b) Schematic diagram of integral area under the voltage–time curve for relative energy consumption calculation.

The relative energy consumption and the HBOR selectivity were calculated based on the electrochemical measurements in a standard H–type cell (**Figure S23**).

The energy consumption (W) is the integral of power (P) over time (t), where $P = V \times I$. Since the current (I) is constant and same for both the HBOR||HER system (HE_{HBOR}) and the OER||HER system (HE_{OER}), the energy consumption is directly proportional to the integral of the voltage over time ($W = I \times \int V\,dt$). The term $\int V\,dt$ represents the area under the voltage–time curve. Therefore, the ratio of the areas under the voltage–time curves represent the relative energy consumption. The relative energy consumption of HE_{HBOR} was calculated to be 14.5% compare to HE_{OER}, confirming the substantial energy–saving achieved by the novel HE_{HBOR} system.

The HBOR selectivity (α) was determined by quantifying the volume of evolved gases at the anode and cathode using a gas collection method. The volume of gas generated at the anode is denoted as V_A, while denoted as V_C at the cathode. The anode gas consists of nitrogen produced from electrochemical HB oxidation and hydrogen generated from partial HB hydrolysis, while the cathode undergoes the hydrogen evolution reaction (HER) to produce hydrogen. Therefore, the theoretical volume of nitrogen produced by the electrochemical reaction at the anode is $V_C/5$, and the volume of hydrogen correspondingly generated from hydrolysis is $V_A - V_C/5$. Accordingly, the selectivity (α) can be calculated according to the following formula: $\alpha = 3V_C/(2V_C+5V_A)$.

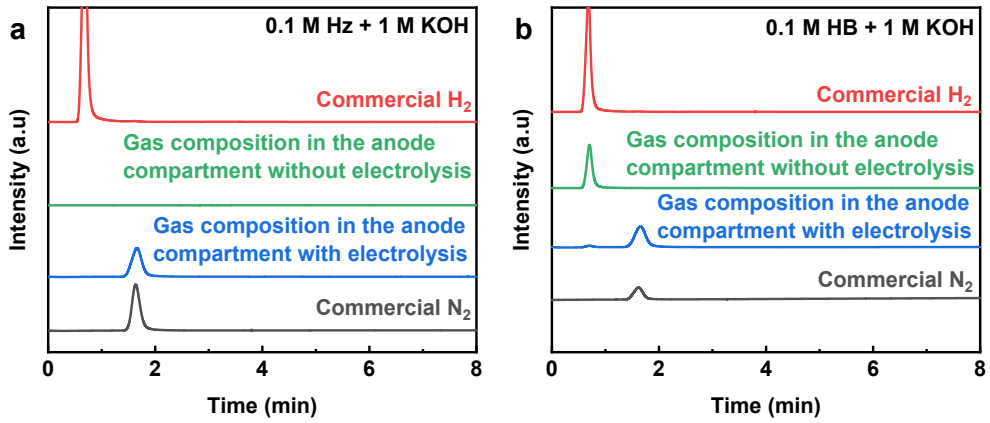

Figure S24. (a) Gas chromatography (GC) analysis results of anode gas products: The electrolyte consists of (a) 0.1 M Hz + 1 M KOH and (b) 0.1 M HB + 1 M KOH.

When the electrolytes are different, the gas phase detection results are similar, except that hydrogen gas is present in the electrolyte containing HB. This indicates that the sulfide catalyst can induce partial slow hydrolysis of BH_3, while N_2H_4 does not undergo spontaneous decomposition.

$$N_2H_4BH_3 + H_2O + OH^- \rightarrow BO_2^- + N_2H_4 + 3H_2$$

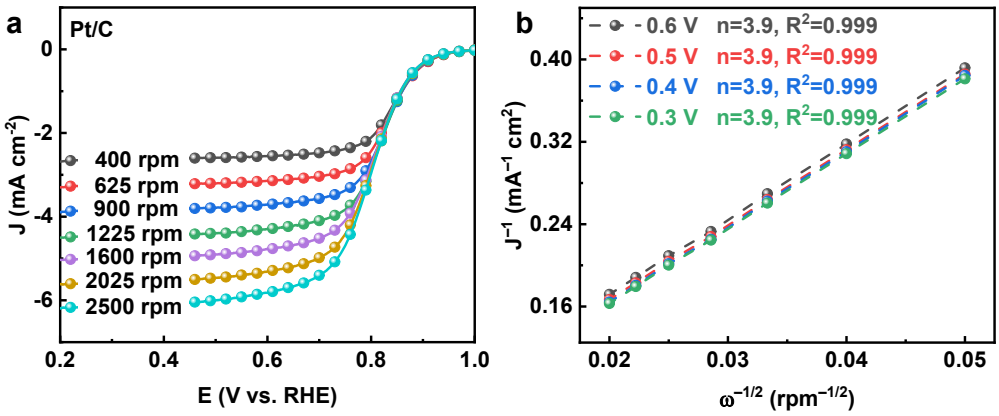

Figure S25. ORR performance of commercial Pt/C.

The electron transfer number (n) is calculated by the Koutecky–Levich equation as follow:[S2]

$$\frac{1}{j} = \frac{1}{j_k} + \frac{1}{j_d}$$

$$j_d = 0.20nFCD^{\frac{2}{3}}v^{-\frac{1}{6}} \cdot w^{\frac{1}{2}}$$

$$j_k = nkFC_{O_2}$$

where j is the measured current density (mA cm^{-2}), j_d is the diffusion limited current density (mA cm^{-2}), j_k is the kinetic current densities (mA cm^{-2}). F is the Faraday constant (96485 C mol^{-1}). D_{O_2} is the diffusion coefficient of O_2 (1.93 × 10^{-5} cm^2 s^{-1}), v is the kinetic viscosity (1.13 × 10^{-2} cm^2 s^{-1}), w is the rotation speed of electrode (rpm), and C_{O_2} is the bulk concentration of O_2 dissolved in 0.1 M KOH (1.2 × 10^{-6} mol mL^{-1}). v (0.01 cm^2 s^{-1}) is the viscosity of the 0.1 M KOH electrolyte solution, and k is the electron–transfer rate constant.

LSV measurements display that the Pt/C exhibits a half–wave potential ($E_{1/2}$) and diffusion limited current density (j_L) of $E_{1/2}$ = 0.808 V and j_L = 5.06 mA cm^{-2} at 1600 rpm (room temperature).

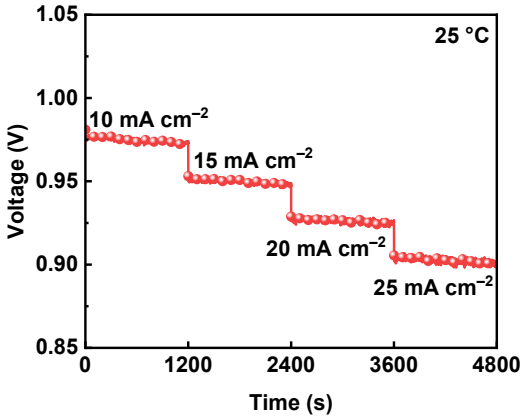

Figure S26. Stability measurements at different current densities of the DHBFC with CoNiFeS (+) || Pt/C (–).

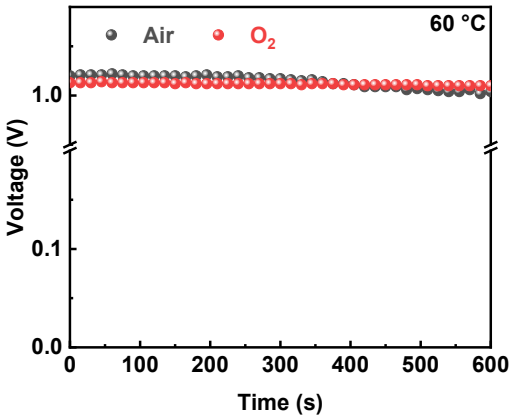

Figure S27. The open–circuit voltage of DHBFC performed at 60 °C.

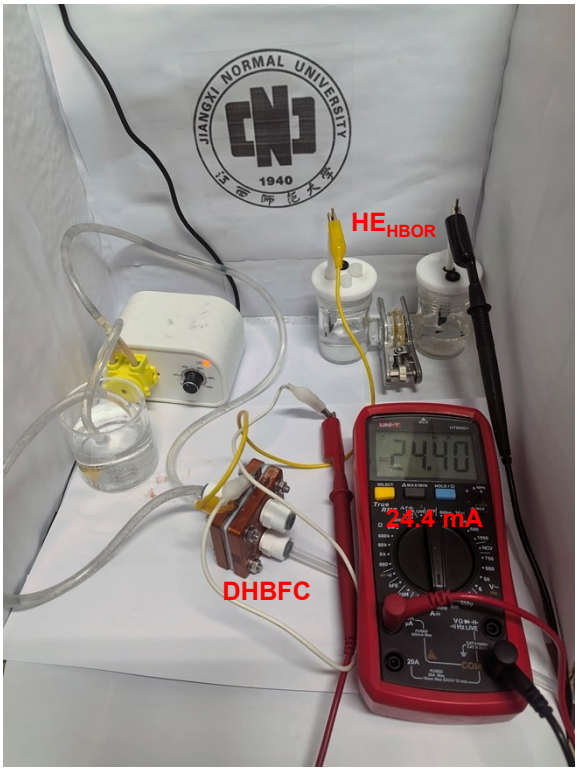

Figure S28. Digital photograph of HE_{HBOR} (CoNiFeS||Pt/C) system for H_2 production self–powered by DHBFC (CoNiFeS||Pt/C).

Table S1. ICP–OES results of CoNiFeS electrocatalyst.

CoNiFeS	No.	wt (%)	average wt (%)	at (%)
Co	1	12.4	12.4	20.6
	2	12.5		
	3	12.4		
Ni	1	24.3	24.3	39.1
	2	24.4		
	3	24.3		
Fe	1	22.1	22.4	40.3
	2	22.5		
	3	22.6		

The value of mole–fraction mixing entropy (S_{mix}) can be used to classify the materials. The S_{mix} can be calculated according to the follow equation.

In the as-prepared CoNiFeS catalyst, Co:Ni:Fe ≈ 1:2:2.

$$S_{mix} = -R\sum_{i=1}^{n} x_n ln\, x_n = 1.06R$$

where n is the number of elemental species, x_n is the mole fraction of component n, and R is the universal gas constant (R = 8.314 J K $^{-1}$ mol $^{-1}$).

Materials with $S_{mix} \geq 1.5R$ are considered to be high–entropy (HE) systems, materials with $1.5R > S_{mix} \geq 1R$ are considered to be medium–entropy (ME) systems, and materials with $S_{mix} < 1R$ are considered to be low–entropy (LE) systems.

Table S2. Binding energies of Co 2p in CoNiFeS and its comparative electrocatalysts.

	CoNiFeS	**NiFeS**	**CoS**
Co–S	779.2/794.2	—	779.1/794.2
Co^{2+}	782.2/797.4	—	782.7/798.7
Sat.	787.2/803.0	—	787.5/803.9

Table S3. Binding energies of Ni 2p in CoNiFeS and its comparative electrocatalysts.

	CoNiFeS	**NiFeS**	**CoS**
Ni–S	854.0/871.3	854.1/871.3	—
Ni^{3+}	856.9/874.5	856.5/874.6	—
Sat.	862.0/879.3	861.4/879.3	—

Table S4. Binding energies of Fe 2p in CoNiFeS and its comparative electrocatalysts.

	CoNiFeS	**NiFeS**	**CoS**
Fe–S	707.5/720.3	707.5/719.7	—
Fe^{3+}	711.3/724.6	710.8/723.9	—
Sat.	714.6/727.7	713.2/727.1	—

Table S5. Binding energies of S 2p in CoNiFeS and its comparative electrocatalysts.

	CoNiFeS	**NiFeS**	**CoS**
S^{2-}	162.9/164.1	162.9/164.1	162.6/163.7
S–O	168.8/169.9	169.0/170.0	169.3/170.4
Sat.	166.1	165.2	164.4

Table S6. OER performance comparison with recently reported electrocatalysts.

No.	Catalyst	Overpotential (mV, J=10 mA cm^{-2})	Tafel (mV dec^{-1})	Ref.
1	**CoNiFeS**	**199**	**56.7**	**This work**
2	$Fe_{0.8}Ni_{0.15}S_{1.05}$	228	53.0	S3
3	Ni–Fe disulfide@oxyhydroxide heterostructure	230	42.6	S4
4	Fe_3O_4/FeS_2/NF	253	48.0	S5
5	$Fe_xNi_{1-x}S_2$ nanosheets	260	46.0	S6
6	Fe–Ni_3S_2/AF	267	36.0	S7
7	Co–NC@$CoFeS_2$	275	62.9	S8

Table S7. Recently reported small–molecule–based coupled electrolyzers.

Anodic catalyst	Electrolyte (substrate + 1 M KOH)	Coupled electrolyzer	V_{cell}@J (V, mA cm^{-2})	Ref.
CoNiFeS	**0.1 M HB**	**HBOR||HER**	**0.051@10 0.08@20 0.176@50**	**This work**
NiCoP@CoFeP	0.1 M HB	HBOR||HER	0.078@10	S9
$Zn_{0.08}Co_{0.92}P$	0.5 M urea	UOR||HER	1.38@10	S10
Ni_3N nanosheets/CC	0.33 M urea	UOR||HER	1.44@10	S11
Cu–α–$Ni(OH)_2$/NF	0.33 M urea	UOR||HER	1.49@10	S12
V–Ni_3N/NS	0.1 M hydrazine	HzOR||HER	0.264@50	S13
Ni–SN@C	0.1 M hydrazine	HzOR||HER	0.366@10	S14
Cu_1Ni_2–N	0.5 M hydrazine	HzOR||HER	0.24@10	S15
$CoSe_2$ nanosheet	0.5 M hydrazine	HzOR||HER	0.164@10	S16
$Co(OH)_2$@HOS/CP	0.5 M methanol	MOR||HER	1.497@10	S17
SA In–Pt NWs/C	0.5 M ethanol	EOR||HER	0.62@10	S18
PtCu nanoframe	0.5 M ethanol	EOR||HER	0.58@10	S19
MoO_x/Pt	0.1 M glycerol	GOR||HER	0.70@10	S20
RhIr/Ti//HEA–CoNiCuMnMo	0.1 M glycerol	GOR||HER	0.55@10	S21
Pt/C//Fe_2P/SS	0.5 M glucose	GOR||HER	1.22@10	S22
$Fe_{0.1}$–$CoSe_2$/CC	0.5 M glucose	GOR||HER	0.72@10	S23

Table S8. Recently reported direct liquid fuel cells.

Anodic catalyst	DLFC	OCV (V)	P_{max} (mW cm^{-2})	Ref.
CoNiFeS	**DHBFC**	**1**	**156**	**This work**
6W–O–CoP/NF	DHzFC	1.1	142	S24
Fe–CoS_2	DHzFC	1.03	125	S25
Ni–Co–P	DHzFC	~1	96	S26
Ni_3N–Co_3N PNAs/NF	DHzFC	~1	60.3	S27
FeNiP–NPHC	DHzFC	0.98	31	S28
RuFe–Ni_2P	DHzFC	~1	60.1	S29
Ru/PNC	DHzFC	1.5/H_2O_2	76.5	S30
Pd–nanoarray@CP	DFAFC	~0.98	35.8	S31
PtRu/C	DFAFC	~0.94	64	S32
$Pd_{0.64}Pt_{0.36}$ NPs	DMFC	＜0.5	99.6	S33
PtRu/C	DMFC	＜0.7	22	S34
H–PtNi@PtSn NWs/C	DMFC	~0.6	65.1	S35
$PtAu_1$SAAs	DMFC	~0.7	155	S36
PtPdAu/BiTe	DMFC	＜0.8	87.2	S37
PtPdAu/BiTe	DEFC	＜0.8	72.9	S37

* The cathode component is assumed to be O_2 with further notation.

Reference

S1. Z. J. Zhang, Z. H. Lu and X. S. Chen, *ACS Sustain. Chem. Eng.*, 2015, **3**, 1255–1261.

S2. S. L. Liu, H. F. Teng, K. Ma, W. X. Miao, X. T. Zhou, X. J. Cui, X. Zhou, L. H. Jiang and B. Y. Xia, *Adv. Mater.*, 2025, **37**, 2508055.

S3. Z. J. Jing, Q. Y. Zhao, D. H. Zheng, L. Sun, J. H. Geng, Q. N. Zhou and J. J. Lin, *J. Mater. Chem. A*, 2020, **8**, 20323–20330.

S4. M. Zhou, Q. H. Weng, X. Y. Zhang, X. Wang, Y. M. Xue, X. H. Zeng, Y. Bando and D. Golberg, *J. Mater. Chem. A*, 2017, **5**, 4335–4342.

S5. M. J. Wang, X. Q. Zheng, L. L. Song, X. Feng, Q. Liao, J. Li, L. Li and Z. D. Wei, *J. Mater. Chem. A*, 2020, **8**, 14145–14151.

S6. X. Y. Ding, W. W. Li, H. P. Kuang, M. Qu, M. Y. Cui, C. H. Zhao, D. C. Qi, F. E. Oropeza and K. H. L. Zhang, *Nanoscale*, 2019, **11**, 23217–23225.

S7. M. Wang, L. Zhang, J. L. Pan, M. R. Huang and H. W. Zhu, *Nano Res.*, 2021, **14**, 4740–4747.

S8. Y. R. Wang, W. Jin, C. J. Xuan, J. Wang, J. Li, Q. Yu, B. B. Li, C. Wang, W. Q. Cai and J. Wang, *J. Power Sources*, 2021, **512**, 230430.

S9. Y. F. Peng, M. S. Huang, Q. F. Yang, Z. Y. Xing and Z. H. Lu, *Inorg. Chem.*, 2023, **62**, 11056–11063.

S10. T. T. Liu, D. N. Liu, F. L. Qu, D. X. Wang, L. Zhang, R. X. Ge, S. Hao, Y. J. Ma, G. Du, A. M. Asiri, L. Chen and X. P. Sun, *Adv. Energy Mater.*, 2017, **7**, 1700020.

S11. Q. Liu, L. S. Xie, F. L. Qu, Z. A. Liu, G. Du, A. M. Asiri and X. P. Sun, *Inorg. Chem. Front.*, 2017, **4**, 1120.

S12. J. F. Xie, L. Gao, S. S. Cao, W. W. Liu, F. C. Lei, P. Hao, X. Y. Xia and B. Tang, *J. Mater. Chem. A*, 2019, **7**, 13577.

S13. J. H. Zhang, Y. Liu, J. M. Li, X. Jin, Y. P. Li, Q. Z. Qian, Y. X. Wang, A. E. Harairy, Z. Y. Li, Y. Zhu, H. K. Zhang, M. Y. Cheng, S. Y. Zeng and G. Q. Zhang, *ACS Appl. Mater. Interfaces*, 2021, **13**, 3881.

S14. H. Y. Jin, X. S. Wang, C. Tang, A. Vasileff, L. Q. Li, A. Slattery and S. Z. Qiao, *Adv. Mater.*, 2021, **33**, 2007508.

S15. Z. Y. Wang, L. Xu, F. Z. Huang, L. B. Qu, J. T. K. A. Owusu, Z. A. Liu, Z. F. Lin, B. H. Xiang, X. Liu, K. N. Zhao, X. B. Liao, W. Yang, Y. B. Cheng and L. Q. Mai, *Adv. Energy Mater.*, 2019, **9**, 1900390.

S16. J. Y. Zhang, H. M. Wang, Y. F. Tian, Y. Yan, Q. Xue, T. He, H. F. Liu, C. D. Wang, Y. Chen and B. Y. Xia, *Angew. Chem. Int. Ed.*, 2018, **57**, 7649.

S17. K. Xiang, D. Wu, X. H. Deng, M. Li, S. Y. Chen, P. P. Hao, X. F. Guo, J. L. Luo and X. Z. Fu, *Adv. Funct. Mater.*, 2020, **30**, 1909610.

S18. Y. M. Zhu, X. R. Zhu, L. Z. Bu, Q. Shao, Y. F. Li, Z. W. Hu, C. T. Chen, C. W. Pao, S. Z. Yang and X. Q. Huang, *Adv. Funct. Mater.*, 2020, **30**, 2004310.

S19. H. Fu, N. Zhang, F. L. Lai, L. S. Zhang, S. L. Chen, H. J. Li, K. Z. Jiang, T. Zhu, F. P. Xu and T. X. Liu, *ACS Catal.*, 2022, **12**, 11402.

S20. X. W. Yu, E. C. Santos, J. White, G. S. Alvarez, L. G. M. Pettersson, A. Cornell and M. Johnsson, *Small*, 2021, **17**, 2104288.

S21. L. F. Fan, Y. X. Ji, G. X. Wang, J. X. Chen, K. Chen, X. Liu and Z. H. Wen, *J. Am. Chem. Soc.*, 2022, **144**, 7224–7235.

S22. P. Y. Du, J. J. Zhang, Y. H. Liu and M. H. Huang, *Electrochem. Commun.*, 2017, **83**, 11–15.

S23. D. D. Zheng, J. W. Li, S. Q. Ci, P. W. Cai, Y. C. Ding, M. T. Zhang and Z. H. Wen, *Appl. Catal. B*, 2020, **277**, 119178.

S24. G. Meng, Z. W. Chang, L. B. Zhu, C. Chen, Y. F. Chen, H. Tian, W. S. Luo, W. P. Sun, X. Z. Cui and J. L. Shi, *Nano–Micro Lett.*, 2023, **15**, 212.

S25. X. J. Liu, J. He, S. Z. Zhao, Y. P. Liu, Z. Zhao, J. Luo, G. Z. Hu, X. M. Sun and Y. Ding, *Nat. Commun.*, 2018, **9**, 4365.

S26. L. B. Zhu, J. Huang, G. Meng, T. T. Wu, C. Chen, H. Tian, Y. F. Chen, F. T. Kong, Z. W. Chang, X. Z. Cui and J. L. Shi, *Nat. Commun.*, 2023, **14**, 1997.

S27. Q. Z. Qian, J. H. Zhang, J. M. Li, Y. P. Li, X. Jin, Y. Zhu, Y. Liu, Z. Y. Li, A. E. Harairy, C. Xiao, G. Q. Zhang and Y. Xie, *Angew. Chem. Int. Ed.*, 2021, **133**,

6049–6058.

S28. Q. P. Yu, X. B. Liu, G. S. Liu, X. P. Wang, Z. J. Li, B. Li, Z. X. Wu and L. Wang, *Adv. Funct. Mater.*, 2022, **32**, 2205767.

S29. X. J. Zhai, Q. P. Yu, J. Q. Chi, X. P. Wang, B. Li, B. Yang, Z. J. Li, J. P. Lai and L. Wang, *Nano Energy*, 2023, **105**, 108008.

S30. X. Y. Guan, Q. N. Wu, H. B. Li, S. Y. Zeng, Q. X. Yao, R. Li, H. Y. Chen, Y. Zheng and K. G. Qu, *Appl. Catal. B*, 2023, **323**, 122145.

S31. Y. Zhou, Y. Yang, X. Zhu, T. Zhang, D. D. Ye, R. Chen and Q. Liao, *Adv. Funct. Mater.*, 2022, **32**, 2201872.

S32. M. Higa, S. Mehdizadeh, S. Y. Feng, N. Endo and Y. Kakihana, *J. Membr. Sci.*, 2020, **597**, 117618.

S33. K. Juchniewicz, I. S. Pieta, B. Mierzwa, M. Pisarek, R. G. Kadam, O. Mozgova, M. Holdynski, A. Malolepszy, A. Borodzinski and P. Pieta, *ACS Sustainable Chem. Eng.*, 2025, **13**, 9609–9620.

S34. W. J. Yuan, C. J. Hou, J. F. Wu, Y. F. Zhang and X. L. Zhang, *Chem. Eng. J.*, 2023, **470**, 143663.

S35. L. Y. Wang, C. H. Zhan, W. Yan, Y. H. Li and L. Z. Bu, *J. Mater. Chem. A*, 2024, **12**, 13458–13465.

S36. S. P. Luo, L. Xie, X. Y. Cai, W. Chen, J. Y. Wu, Y. T. Ding, Y. S. Zhou, Z. W. Quan, R. F. Feng, X. Z. Fu and J. L. Luo, *Adv. Mater.*, 2025, **37**, 2500848.

S37. T. T. Zhou, K. Y. Dong, Z. Zheng and Q. Yuan, *Rare Met.*, 2025, **44**, 3119–3129.